Materials and Design 189 (2020) 108505

Contents lists available at ScienceDirect

Materials and Design

journal homepage: www.elsevier.com/locate/matdes

Gas tungsten arc welding of as-rolled CrMnFeCoNi high entropy alloy

J.P. Oliveira [a,*], T.M. Curado [a], Z. Zeng [b], J.G. Lopes [a], Emma Rossinyol [c], Jeong Min Park [d], N. Schell [e], F.M. Braz Fernandes [f], Hyoung Seop Kim [e,g]

[a] UNIDEMI, Department of Mechanical and Industrial Engineering, NOVA School of Science and Technology, Universidade NOVA de Lisboa, 2829-516 Caparica, Portugal
[b] School of Mechanical and Electrical Engineering, University of Electronic Science and Technology of China, Chengdu 221116, China
[c] Servei de Microscòpia, Universitat Autònoma de Barcelona, E-08193 Bellaterra, Spain
[d] Department of Materials Science and Engineering, POSTECH (Pohang University of Science and Technology), Pohang 790-784, South Korea
[e] Helmholtz-Zentrum Geesthacht, Institute of Materials Research, Max-Planck-Str. 1, Geesthacht 21502, Germany
[f] CENIMAT/I3N, Department of Materials Science, Faculty of Sciences and Technology, Universidade NOVA de Lisboa, Caparica 2829-516, Portugal
[g] Center for High Entropy Alloys, POSTECH (Pohang University of Science and Technology), Pohang 790-794, South Korea

HIGHLIGHTS

- Gas tungsten arc welding of as-rolled CrMnFeCoNi high entropy alloys is performed.
- Defect-free joints with good mechanical behaviour were obtained.
- Synchrotron X-ray diffraction was used to study the texture and microstrain along the joint.
- Arc-based welding techniques are suitable for welding these novel advanced engineering alloys.

GRAPHICAL ABSTRACT

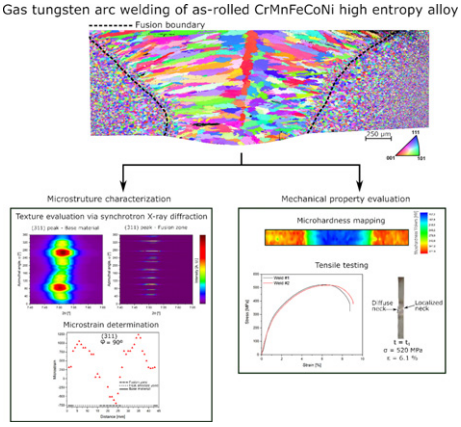

ARTICLE INFO

Article history:
Received 7 December 2019
Received in revised form 6 January 2020
Accepted 15 January 2020
Available online 16 January 2020

Keywords:
High entropy alloys
CrMnFeCoNi
Gas tungsten arc welding
Synchrotron X-ray diffraction
Recovery
Mechanical testing

ABSTRACT

High entropy alloys have emerged as novel engineering alloys with remarkable mechanical properties in a wide range of temperatures. Among the several high entropy alloys that were already described, the equiatomic CrMnFeCoNi alloy is the most studied one. In this work, gas tungsten arc welding of as-rolled CrMnFeCoNi high entropy alloy sheets was performed. The microstructural characterization encompassed the use of electron microscopy, including electron backscattered diffraction, synchrotron X-ray diffraction analysis, microhardness testing and mechanical evaluation. A comprehensive description of the microstructural evolution, including texture and microstrain determination, of the joint is presented and discussed. Upon mechanical testing, the joints systematically failed in the fusion zone due. The large grain size and low hardness of this region justifies the failure location. The joints' mechanical behaviour is correlated with the material microstructure.

* Corresponding author.
E-mail address: jp.oliveira@fct.unl.pt (J.P. Oliveira).

https://doi.org/10.1016/j.matdes.2020.108505

1. Introduction

High entropy alloys are a new class of advanced engineering alloys which have been attracting significant attention, due to the possibility of controlling their composition, microstructure and resulting mechanical performance [1]. Typically, these materials are composed of at least five principal elements, with a concentration varying between 5 and 35 at.% [2].

The concept of high entropy alloy was presented in 2004 by the independent works of Cantor et al. [3] and Yeh et al. [4]. These extraordinary materials exhibit four core effects: (i) high-entropy effect, which is related to the system configuration entropy; (ii) sluggish diffusion, in which diffusion-based phenomena are slower than in conventional engineering alloys, thus improving the high temperature properties; (iii) severe lattice distortion, caused by the existence of at least five atoms (following the conventional definition of high entropy alloys) which may have significantly different sizes; (iv) and the cocktail effect, where the addition of specific elements can drastically improve a particular property of the alloy.

The equiatomic CrMnFeCoNi alloy presented in [3] is, so far, the most studied composition [5–11]. This alloy composition yields a single phase FCC solid solution, due to the high configurational entropy of the system [12] and is known to present excellent mechanical properties even at sub-zero temperatures [13].

Upon the development of any engineering alloy their thermomechanical processability must be studied. One key manufacturing processing often used in structural applications is welding. Welding allows the creation of structures shaped in a complex manner from simple monolithic parts, but also can be used to join materials with different properties [14,15].

Currently, some studies have addressed the weldability of the CrMnFeCoNi high entropy alloy. Among the different welding techniques available, laser welding has received more attention [16–21]. Though laser welding is often used due to the reduced size of its heat source [22,23] the high initial investment costs can be a deterrent for its use. In opposition, arc-based welding techniques, such as gas tungsten arc welding are low-cost alternatives yet capable of producing defect-free and highly performant joints provided that the process parameters are optimized [24–26]. Though most research works on welding of the CrMnFeCoNi high entropy alloy use fusion-based methods, solid-state ones have also been used with success to join these materials [27–29].

In any fusion-based welded joint three distinct regions can be observed: the fusion zone, the heat affected zone and the base material. The fusion zone is typically easily recognized by showing coarse grain size and a dendritic-like structure. In the heat affected zone, the material can experience solid-state transformations, such as grain growth, recrystallization and precipitation of new phases.

Typically, identification of the heat affected zone is performed via microscopy techniques [30–32], to assess the grain size and morphology evolution as a function of weld thermal cycle at a given distance from the joint centreline. Another widely used manner for identification of the heat affected zone is through hardness testing [33,34]. Here, there is often a clear distinction between the (micro)hardness of the fusion zone, heat affected zone and base material. By definition, the base material does not experience any solid-state transformation, thought its temperature increases during welding.

As it will be shown in this work, scanning electron microscopy and microhardness testing may not always be enough to effectively determine the extension of the heat affected zone, especially in severely deformed materials. This is due to the occurrence of recovery phenomena, which require low temperatures for onset, especially when the material to be welded was previously (highly) deformed. These recovery phenomena will lead to microstructural changes, such as stress relieving, that are neither detected by conventional microscopy techniques nor hardness measurements. However, such microstructure changes can be determined via X-ray diffraction methods, provided that the experiment can provide high angular resolution with low background noise. This can be accomplished by using synchrotron radiation sources, in which the beam brilliance is extremely higher when

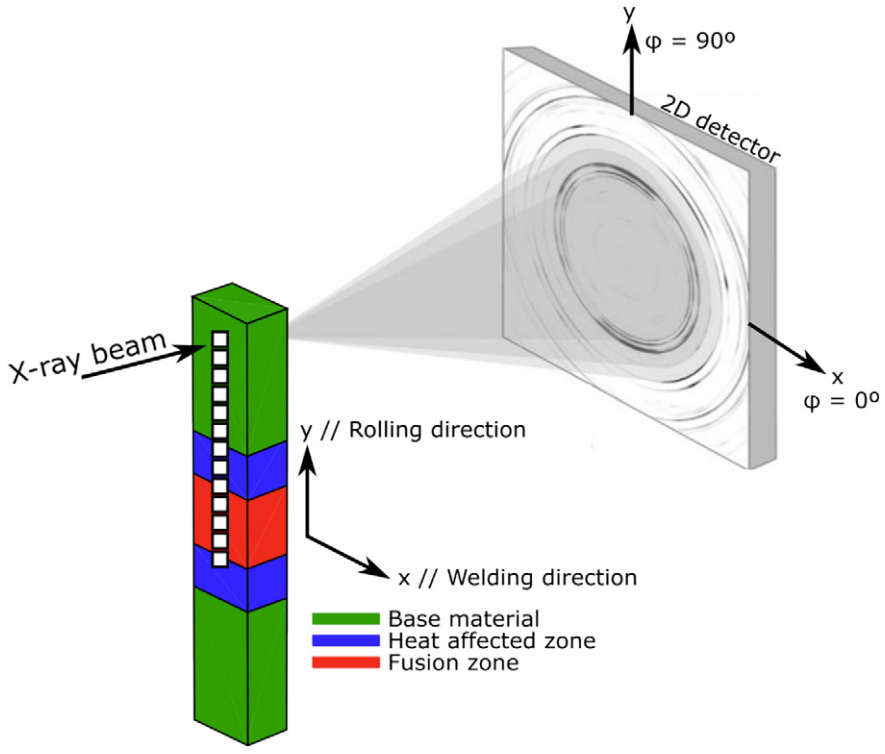

Fig. 1. Setup (not to scale) used for the synchrotron X-ray diffraction experiments. The sample to detector distance was of 1396 mm and an X-ray wavelength of 0.14235 Å was used. The rolling and welding directions are also presented.

compared to conventional laboratory equipment [35,36]. As a result, there is a greater precision on the diffracted beam captured by the detector. Additionally, the typically higher beam energy allows to work in transmission mode, enabling to retrieve bulk microstructural information [37] rather than only surface and subsurface information, obtained when working in reflection mode [38,39].

Gas tungsten arc welding of an as-rolled CrMnFeCoNi high entropy alloy was performed. The microstructural evolution of the as-welded joints was studied by electron microscopy techniques, microhardness mapping and high energy synchrotron X-ray diffraction analysis. Furthermore, the joints mechanical properties were tested. A correlation between the joint microstructure and its mechanical behaviour is established. The massive interest in these novel advanced engineering materials requires the understanding of how the microstructure evolves and influences the mechanical properties upon thermo and/or mechanical processing. We address the concomitant effect of processing-microstructure-properties in this work.

2. Materials and methods

In this work, an as-rolled equiatomic CrMnFeCoNi high entropy alloy, which was cold-rolled at room temperature with a thickness reduction of ≈50% (from 3 mm to 1.5 mm) from the hot-rolled plates, was used as the base material. Prior to welding, parts with $30 \times 30 \times 1.5$ mm were cut using a precision cutting machine. Additionally, the material was mechanically polished to remove the surface oxide, followed by cleaning with ethanol and acetone.

Gas tungsten arc welding was performed using a TELWIN, model Technology TIG 182 AC/DC-HF/LIFT equipment. Welding was performed using direct current and straight polarity so that full penetration and defect-free joints could be obtained. Pure Ar (99.9999%) at a flow rate of 16 L/min was used as shielding gas to prevent oxidation of both the fusion and heat affected zones. After preliminary trials, the following welding parameters were selected: current of 60 A, voltage of 9.2 V and travel speed of 4.2 mm/s. The resulting heat input was of 131.4 J/mm. The welding direction was set normal to the rolling direction. After welding, 3 mm wide strips were prepared using electric discharge machining for microstructural and mechanical characterization.

For microstructural characterization, samples were polished following conventional metallographic preparation techniques. Scanning electron microscopy (SEM) analysis was performed using a JEOL JSM-7800F PRIME high-resolution field emission SEM equipped with dual energy-dispersive X-ray spectroscopy (EDS) and backscattered electron (BSE) detectors. Moreover, in order to quantitatively investigate the morphological and crystallographic texture of the specimens, electron backscattered diffraction (EBSD) analysis was conducted using FEI XL-

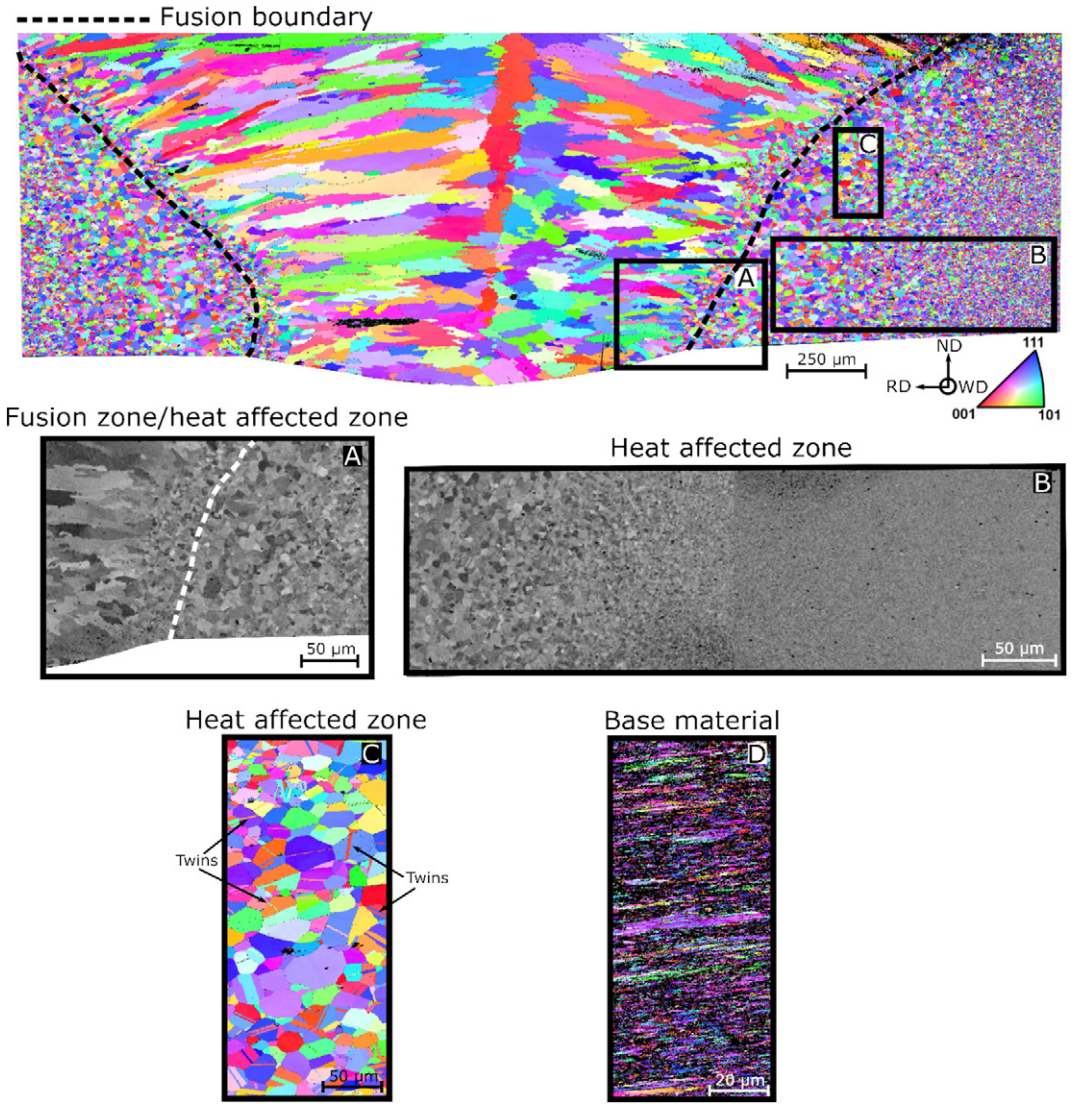

Fig. 2. Scanning electron microscopy aided by electron backscattered diffraction images of the CrMnFeCoNi high entropy alloy welded joint. The inverse pole figure is parallel to the welding direction (WD).

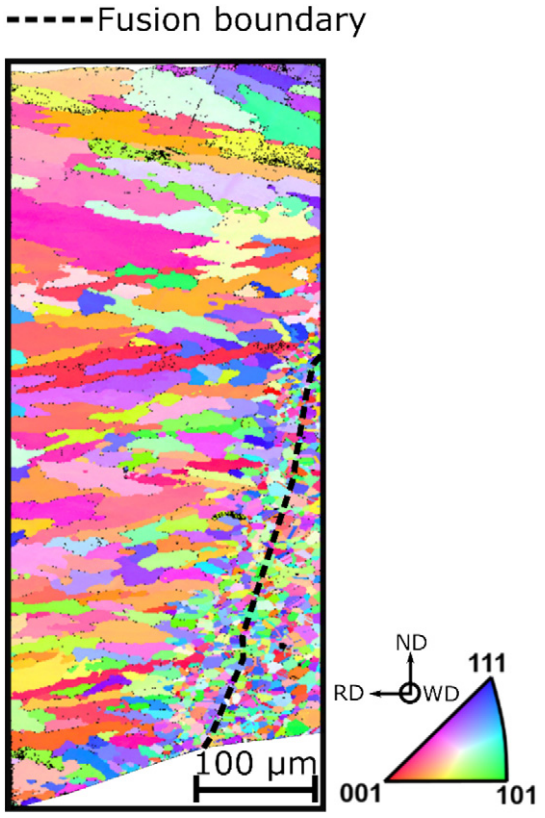

Fig. 3. Electron backscattered diffraction image of the fusion zone/heat affected zone interface, with the inverse pole figure parallel to the rolling direction (RD).

30S FEG SEM. Analysis of the orientation imaging microscopy (OIM) was performed using TSL OIM Analysis 7.

Synchrotron X-ray diffraction analysis was performed at P07 beamline at PETRAIII/DESY. The setup used for the diffraction experiments is depicted in Fig. 1. Considering the sample orientation relatively to the laboratory referential, the azimuth angle, ϕ, is 0° in the longitudinal direction of the fusion zone, and perpendicular to it at $\phi = 90°$. Note that the welding direction is parallel to the 0° azimuthal angle. Working in transmission mode, with an energy of 87.1 keV (corresponding to a wavelength of 0.14235 Å), the welded joints were scanned from the base material towards the heat affected zone and fusion zone, finishing on the other side of the base material. The beam spot size was set to 200 × 200 μm, with a 200 μm step between consecutively analysed spots. The sample to detector distance was fixed at 1396 mm. The Debbye-Scherrer rings were captured using a 2D Perkin Elmer XRD 1622 fast detector. The raw data was treated using freely available Fit2D software [40,41] following the procedure adopted in [42]. Full integration along the azimuthal angle ϕ, i.e. from 0 to 360°, was performed to determine the existing phases along the welded joints.

To evaluate the microstructural dependence on the crystallographic orientation, analysis of the full width at half maximum (FWHM) and of the microstrain along the welded joints at $\phi = 0°$ (from −5 to 5°) and $\phi = 90°$ (from 85 to 95°) azimuthal angles (refer to Fig. 1), was performed. These azimuthal angles correspond to the principal directions of the sample: with 0° being the *x* component, along the longitudinal direction of the fusion zone; and 90° the *y* component, along the transverse direction of the fusion zone. Because of the reduced thickness of the analysed material, the strain along this direction can be considered negligible [43]. The instrumental peak broadening, which can affect the FHWM results, was considered by using a LaB_6 calibration standard.

For both the FWHM and microstrain analysis the (311) diffraction peak was selected, since it is known that for FCC structures such family of planes has low symmetry and is insensible to intergranular strains [44,45]. The microstrain, $\varepsilon_{(311)}$, was calculated using Eq. (1):

$$\varepsilon_{(311)} = \frac{d_{(311)} - d_{0(311)}}{d_{0(311)}}, \quad (1)$$

where $d_{(311)}$ is the d-spacing at each analysed position of the joint for the (311) diffraction peak and $d_{0(311)}$ is the corresponding stress-free d-spacing obtained from the same alloy ingot but in the annealed condition. The $d_{(311)}$ values for the 0 and 90° azimuthal angles were determined by peak fitting using a pseudo-Voigt function, which is suitable for synchrotron radiation sources [46].

Microhardness mapping across the base material, heat affected and fusion zones was performed along a cross-section perpendicular to the welding direction using a Mitutoyo Micro Hardness Testing Machine HM-112. A load of 0.5 kg, held during 10 s, was used for the indentation process. The space between consecutive indentations in both the longitudinal and transverse directions was set to 200 μm.

Tensile testing was performed to evaluate the mechanical properties of the as-welded material. An Autograph Shimadzu AG50kNG machine equipment with a 50 kN load cell was used. The displacement rate was set to 1 mm/min. The tensile force was applied perpendicularly to the welding direction. The gauge length of the samples was 30 mm with a cross-section of 3 × 1.5 mm. A total of three welded specimens were tested to observe the consistency of the obtained mechanical data. The fracture surfaces were observed by SEM.

3. Results and discussion

3.1. Microstructure

Full penetration, defect-free joints were obtained as observed by SEM aided with EBSD (refer to Fig. 2). The inserts in the inverse pole figure (IPF) map, corresponding to regions A to C, are also characterized by SEM imaging. Note that region D, corresponding to the rolled base

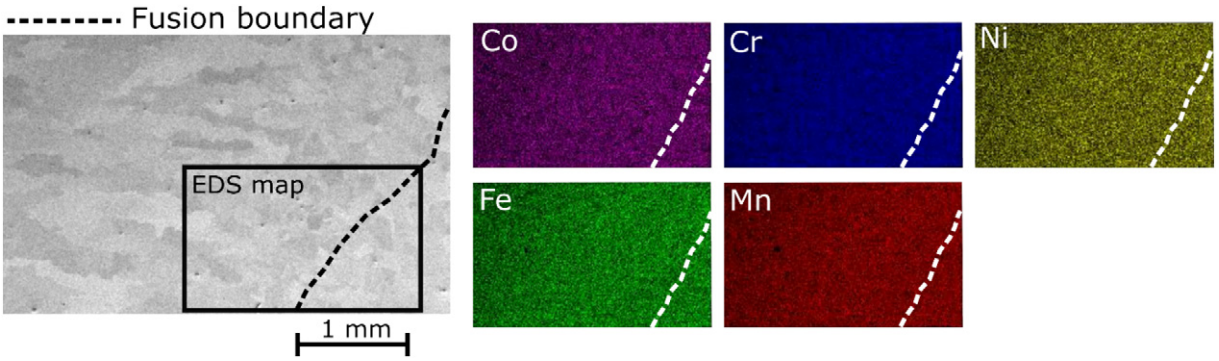

Fig. 4. EDS mapping across the fusion zone and heat affected zone.

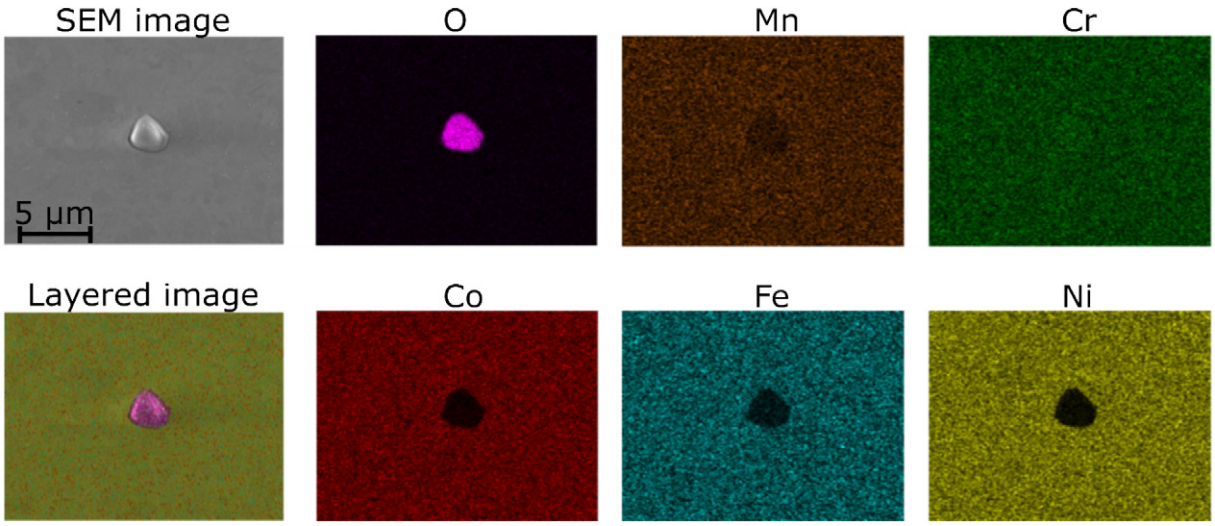

Fig. 5. EDS mapping of an inclusion found in the heat affected zone of the welded joint.

material, is not presented in the major EBSD map of the welded joint owing to the large dimensions of the as-welded samples. Additionally, the IPF maps in Fig. 2 are shown parallel to the welding direction (WD).

The base material, heat affected zone and fusion zone are characterized by different microstructural features. In the base material (region D), pancaked shaped grains with a width of ≈2 μm exist. In the heat

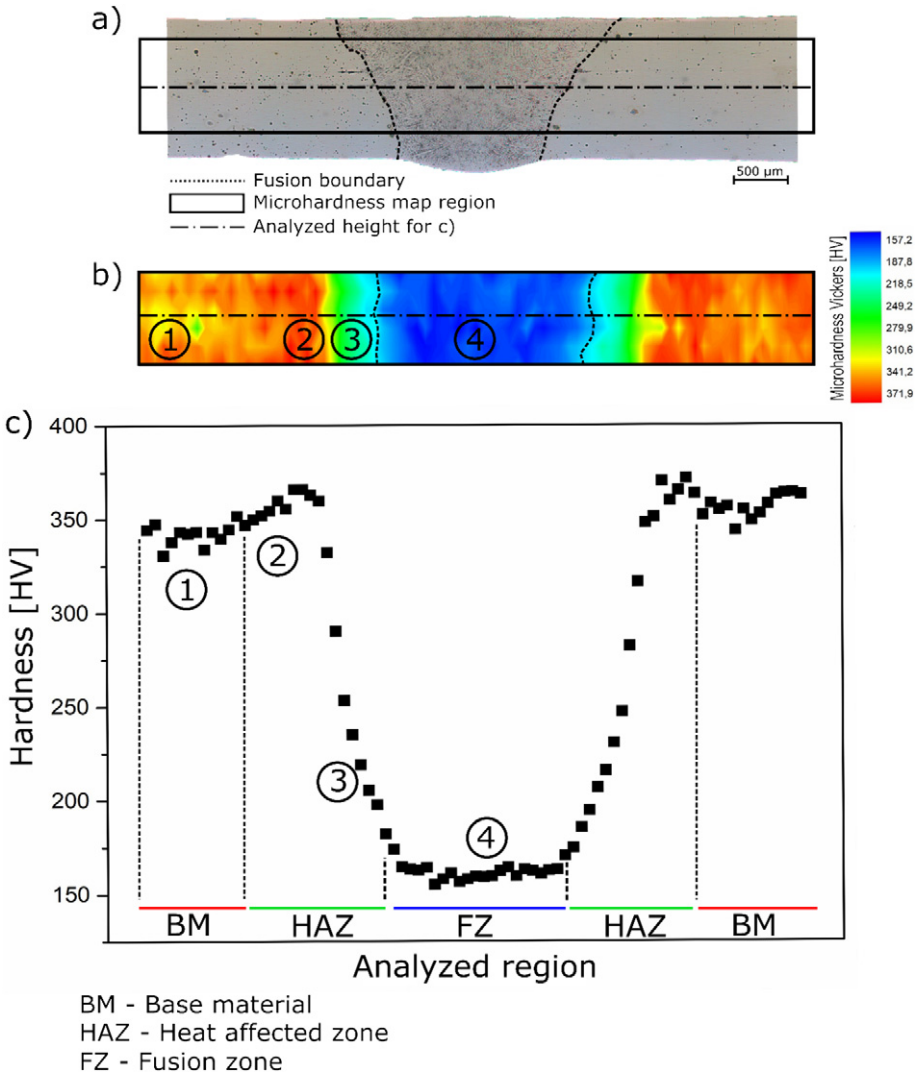

Fig. 6. a) Optical micrograph of the as-welded CrMnFeCoNi high entropy alloy; b) colorized microhardness map; c) microhardness evolution at mid height of the welded joint.

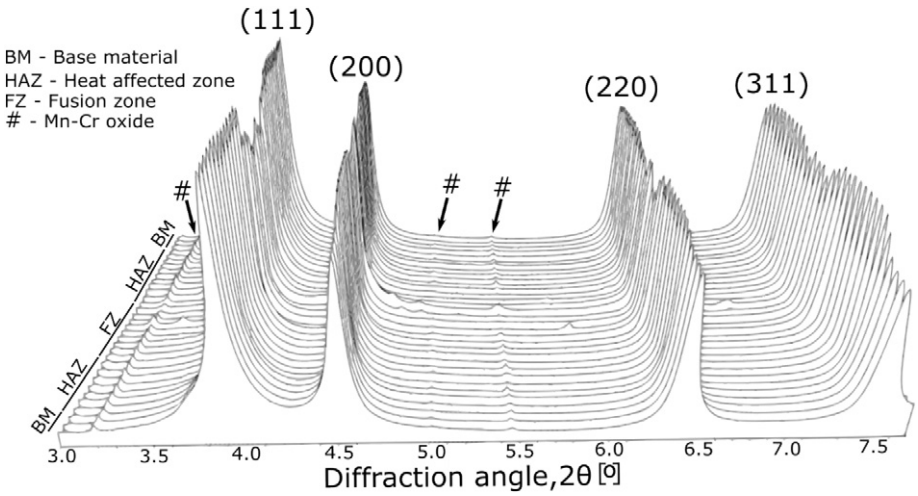

Fig. 7. Superimposition of the diffraction patterns obtained after full integration (360°) of the Debbye-Scherrer rings along the azimuthal angle.

affected zone (region B) the grain size increases, when compared to the base material. From the base material/heat affected zone interface towards the fusion boundary, grain growth is observed. However, the average grain size near the base material/heat affected zone boundary and near the fusion boundary greatly differs. In the latter region, the grain size approaches ≈30 μm, while for the former this value decreases to ≈5 μm. These differences in grain size within the heat affected zone can be explained based on the thermal cycle experienced by the material during welding. It is known that the peak temperature is higher at the weld centreline and decays towards the base material [47]. This decay will depend on the heat input and/or the existence of pre- or post-heating of the material being welded. In the heat affected zone near the fusion boundary (regions A and C), the peak temperature and the permanence time at temperatures which can promote grain grow, are higher and longer, respectively, than near the interface with the base material. Because this solid-state transformation depends

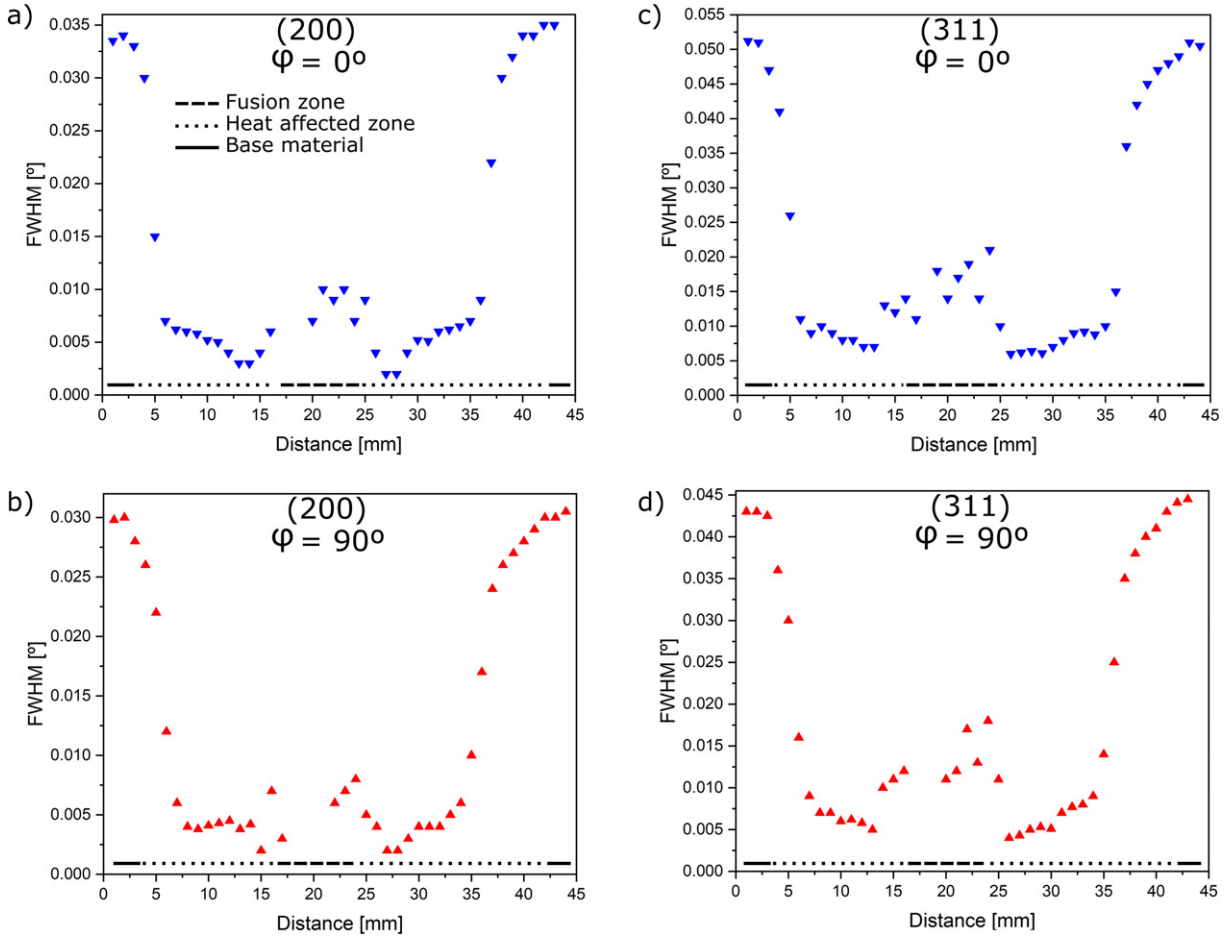

Fig. 8. Evolution of the FWHM for the CrMnFeCoNi welded joints considering the (200) and (311) diffraction peaks near the 0 and 90° azimuthal angles.

exponentially with temperature, it is then expected that the grain size is significantly larger near the fusion boundary rather than near the base material interface, as it was observed in the SEM images of the cross section of the as-welded CrMnFeCoNi high entropy alloy.

At the weld centreline, very large grains, i.e. >50 μm in length, are observed. These columnar grains start to grow in an epitaxially mode from the solid substrate in the heat affected zone and progress to the centre of the fusion zone. Grain growth is known to occur along the direction of maximum temperature gradient which is perpendicular to the liquid/solid interface, according to the common theory of solidification in metals [48,49]. The first grains to solidify are those at the interface with the heat affected zone. Here, grain nucleation is favoured by the cold substrate, which results in several fine and equiaxed grains. However, competitive growth will occur when solidification is proceeding towards the weld centreline. Grains whose preferential growth direction is normal to the melt pool boundary or, equivalently, parallel to the maximum temperature gradient, will prevail over those which have different growth directions. For FCC crystal structures the preferential growing direction is along the ⟨100⟩ direction. According to the EBSD data for the heat affected zone/fusion zone interface depicted in Fig. 3, where the IPF map is shown with the crystal orientation parallel to rolling direction (RD), the columnar grains have a near ⟨100⟩ crystallographic orientation, thus in good agreement with the solidification theory of FCC structures [47]. As it will be shown latter, the different microstructural features observed in both the heat affected and fusion zones will influence the mechanical properties of the as-welded joints.

Other microstructural features can be also observed within the heat affected zone, namely the existence of annealing twins (see detail of region C in Fig. 2). In the fusion zone, no evidence of such microstructural feature is observed.

Energy dispersive spectroscopy mapping of the fusion zone revealed that the elemental distribution across this region is relatively even (Fig. 4), in good agreement with recent works on laser welding of the same CrMnFeCoNi high entropy alloy [21].

In the base material, heat affected zone and fusion zone inclusions were found. These are oxides, mainly enriched in Cr and Mn, as depicted in the energy dispersive spectroscopy maps of Fig. 5. Such precipitates are often found during production of CrMnFeCoNi high entropy alloys and its formation on the base material and heat affected zone is attributed to a potential contamination of the raw materials used during casting of the alloy [50]. In the fusion zone, despite the use of shielding gas to avoid oxidation, the high temperatures reached during welding can also promote such phenomenon. Though oxidation-free welds are often desired, its occurrence is not necessarily detrimental for the material mechanical properties [51].

The results of microhardness mapping across the welded joint are depicted in Fig. 6. Four different regions are identified. In the base material (region 1), as expected owing to the significant deformation imposed during cold rolling of the high entropy alloy, a high hardness is found (≈350 HV). Two regions (2 and 3) compose the heat affected zone. First, in region 2, there is a slight increase in hardness to around 375 HV due to recrystallization phenomena, which decreases grain size. Then, in region 3, grain growth starts to occur and, consequently, hardness started to decrease. This decrease in hardness is more noticeable when approaching the interface with the fusion zone, since closer to the fusion boundary the peak temperature and permanence time

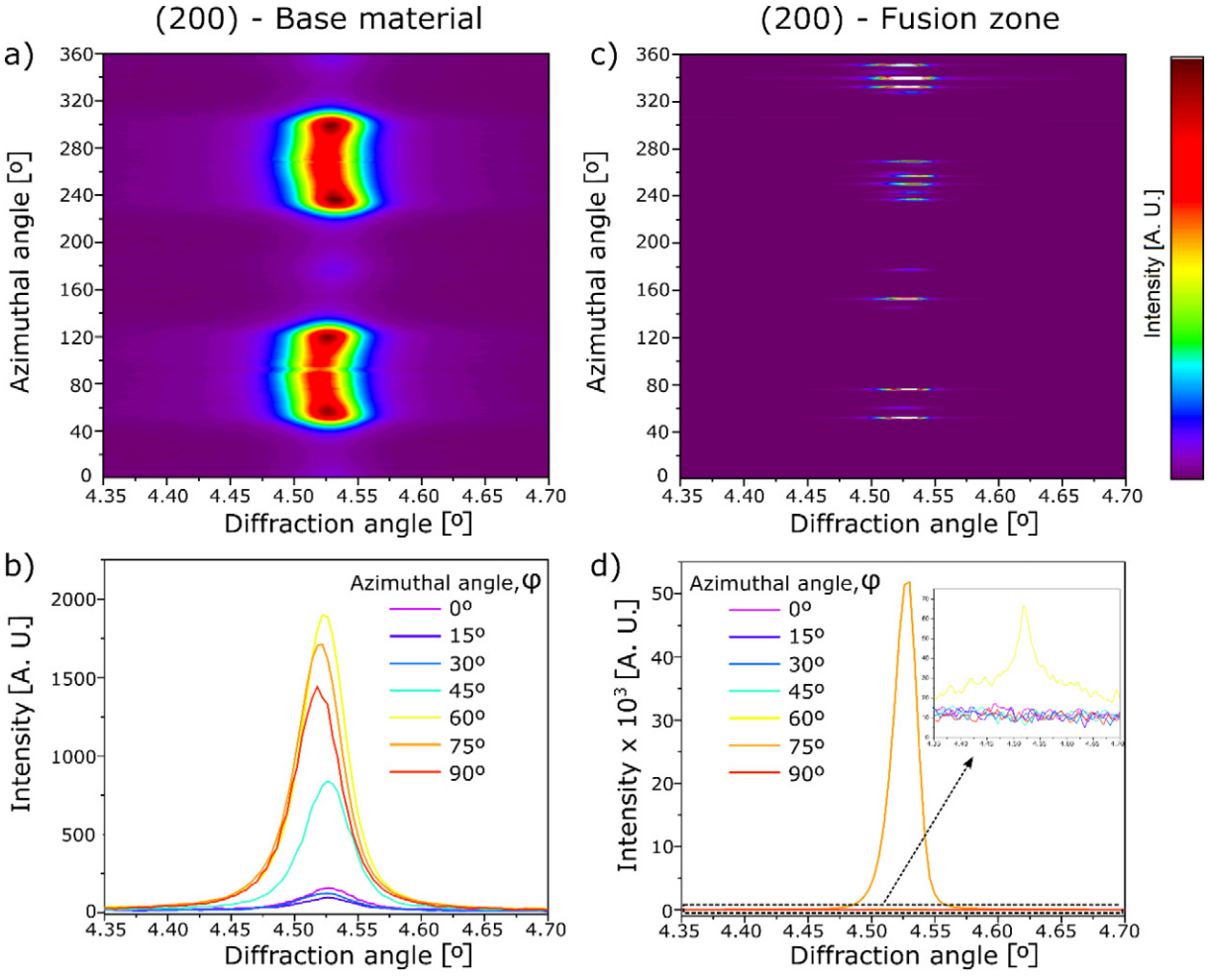

Fig. 9. Variation of the (200) peak position with the azimuthal angle for the base material (a and b) and fusion zone (c and d).

for grain grow are higher. When entering the fusion zone (region 4), the lowest hardness of ≈150 HV is observed. Upon a melting, any previous thermomechanical process experienced by the material is lost. As such, the hardness in the fusion zone is similar to that typically found in as-cast CrMnFeCoNi high entropy alloys [11]. It must be noticed that the refined grain structure of the fusion zone adjacent to the fusion boundary gives rise to a slightly higher hardness (≈165 HV) compared to the weld centreline. The hardness evolution along the mid height of the joint cross section, depicted in Fig. 6c), clearly shows the spatial variation as function of the position in the welded joint.

Laplanche et al. [52] studied the effect of heat treatments after deformation on a CrMnFeCoNi high entropy alloy. It was shown that higher heat treatment temperatures lead to a significant decrease in hardness, whereas low temperatures, i.e., below 530 °C, promoted a slight increase in the material hardness. The current microhardness results are with good agreement with Laplanche et al. [52] work: closer to the fusion boundary (which would correspond to higher heat treatment temperatures) a significant reduction in hardness occurred; near the base material (corresponding to lower heat treatment temperatures) a slight increase in hardness, compared to the highly deformed material, is observed. Overall, it can be stated that the Hall-Petch relation is followed.

Synchrotron X-ray diffraction analysis was performed along the welded joint starting on the base material, crossing the heat affected and fusion zones and finishing on the opposite side of the base material. The 3D view of the diffraction patterns along those regions is depicted in Fig. 7. The diffraction patterns obtained from the integration along the full (360°) azimuthal angle reveals the FCC phase, with the (111), (200), (220) and (311) crystallographic planes, throughout the material. Minor diffraction peaks are also observed in the joint (marked with #). These were identified as Mn- and Cr-based oxides and their presence is in good agreement with the electron microscopy observations. The intensity of the diffraction peaks corresponding to the oxides in the fusion zone is slightly larger than those in the base material and heat affected zone. This can be attributed to a higher volume fraction of oxides in the fusion zone. However, from the microscopy analysis of the joints, the fraction of oxides is of ≈1% in the base material and heat affected zone, with a minor increase to ≈2% in the fusion zone. Due to this reduced volume fraction, the microhardness of the fusion zone is not significantly affected, as it has the typical hardness value of a cast CrMnFeCoNi high entropy alloy [11]. The size of those oxides ranges from around 1 μm in the base material up to 3 μm in the fusion zone. No second phases were formed in the heat affected and fusion zone, potentially due to the short weld thermal cycles and good microstructural stability of the alloy [53]. As such, it can be stated that, overall, the welding procedure did not change the stable phase in joint.

In order to further understand the microstructural evolution based on the synchrotron X-ray diffraction results, the Debbye-Scherrer rings were integrated near the 0 and 90° angles, which correspond to the principal directions of our reference system (refer to Fig. 1).

Analysis of the evolution of the full width at half maximum (FWHM) for the (200) and (311) diffraction peaks along the welded joint is depicted in Fig. 8, and it allows to put in evidence other interesting

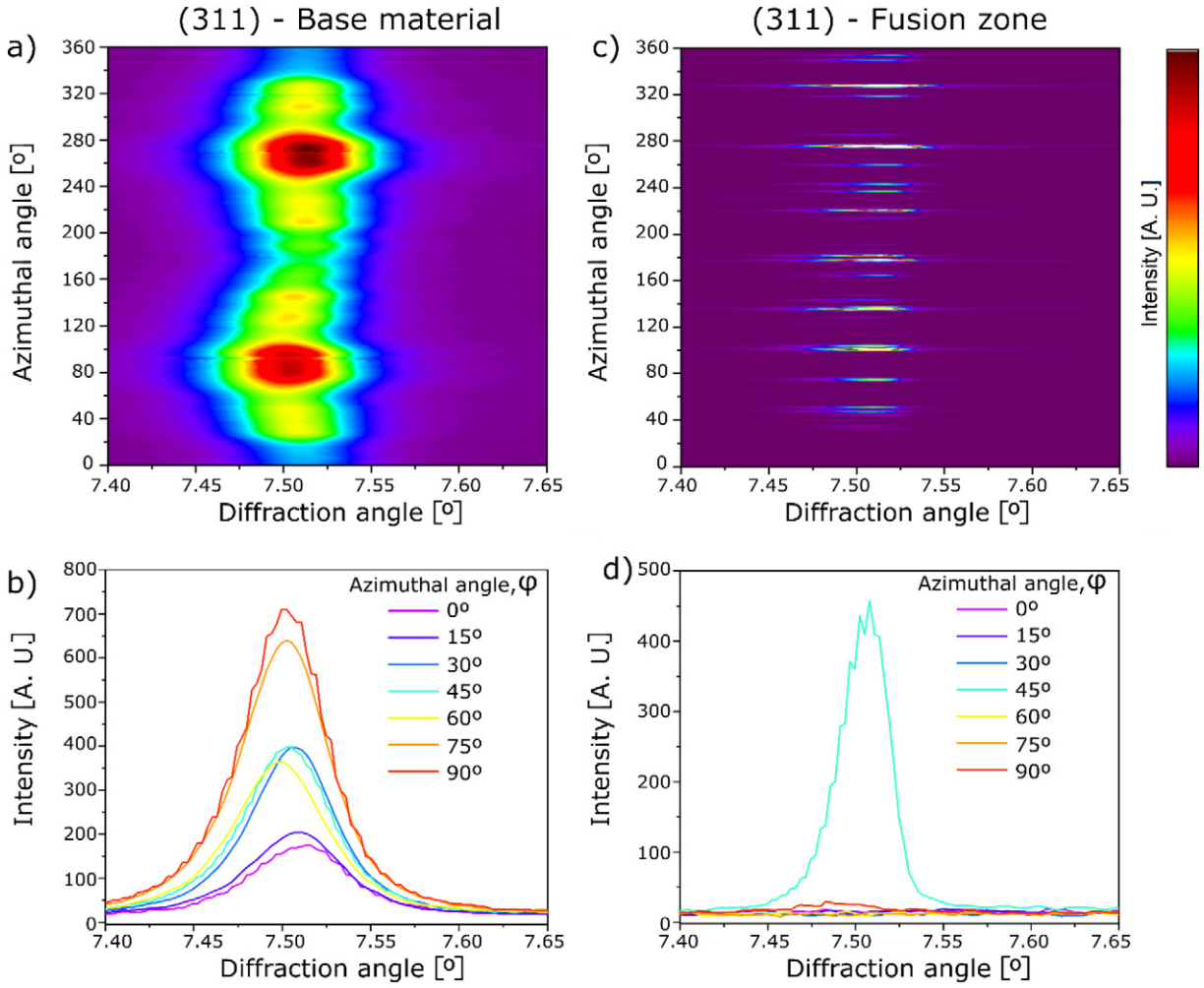

Fig. 10. Variation of the (311) peak position with the azimuthal angle for the base material (a and b) and fusion zone (c and d).

microstructural features induced by the welding process. In fact, along the x (welding) direction, corresponding to $\phi = 0°$ integration, the diffraction peaks in the fusion zone are mainly from the {311} family of planes. A similar situation is observed along the y (perpendicular to the weld bead) direction. The large grain size in the fusion zone, renders that for some azimuthal ranges there are no diffraction patterns for certain families of planes. For example, in Fig. 8a) and b), the (200) diffraction peak is inexistent in some regions of the fusion zone. The same occurs for the (111) and (220) peaks (not shown here to avoid overpopulation of graphs). This marked texture effect is induced by the welding process, only impacts the fusion zone microstructure, and arises from the highly directional solidification conditions imposed upon cooling of the fusion zone but also due to the large grain size existing in this region.

Analysis of the (200) and (311) diffraction peaks along the complete azimuthal angle range (360°) in cartesian coordinates is depicted in Figs. 9(a and c) and 10(a and c) for both base material and centre of the fusion zone, respectively. A similar representation is shown in b and d of Figs. 9 and 10, where the (200) and (311) diffraction peaks are plotted for specific azimuthal angles of 0, 15, 30, 45, 60, 75 and 90°. Both types of results clearly depict that the texture in the base material and fusion are significantly different. In the base material, the (200) diffraction peak has intensity reinforcements from 45 to 90° (considering only the first quadrant of the Debye-Scherrer diffraction images), whereas for the fusion zone only sporadic diffraction occurs. An extremely high diffracted intensity of the (200) peak in the fusion zone occurs at a ϕ angle of 75° (see insert of Fig. 9d). The reason for such high and sporadic intensity at specific azimuthal angles is related to the large grain size of the fusion: once one grain in the fusion zone is in diffraction condition, its diffracted intensity will be necessarily high owing to its large dimension.

It should be emphasized that the abovementioned procedure of integrating the Debbye-Scherrer rings along specific azimuthal angles, instead of using only the full integration results, enables to retrieve direction-specific crystallographic information of any region of the joint. By only considering the full integration results, one could be misled and assume that diffraction of the FCC phase of the CrMnFeCoNi high entropy alloy would always occur in the fusion zone, regardless of the analysed direction. As it was evidenced, this is not the case for certain directions owing to the strong texture effect created by the welding process.

The analysis of the evolution of the FWHM along the welded joints also allows to infer that the actual extension of the heat affected zone is slightly larger than previously considered, based solely on the microhardness measurements. In fact, it is possible to see that the FWHM values obtained upon integration of the (311) peak at $\phi = 90°$ is of ≈0.0425° in the base material (refer to Fig. 8d). Entering the heat affected zone this value immediately drops to ≈0.0357°. However, this region in the microhardness measurements still had the same hardness as the as-received rolled base material. As such, the weld thermal cycle is promoting a microstructural change, which translates in a variation of the FWHM, but not necessarily on the hardness and/or material grain size.

In fact, these synchrotron X-ray diffraction results allow to put in evidence a recovery phenomenon on the severely cold-worked base material. This recovery phenomenon translates into a stress relaxation of the material, which is not reflected in a variation of the grain size neither a significant change in the microhardness values, hence the reason why the use of these two characterization techniques render (slightly) different extensions of the heat affected zone. These results show that, depending on the material to be welded and its original condition, the effective extension of the heat affected zone can vary. Since microhardness testing and optical/electron microscopy are the most used techniques for identification of the heat affected zone, it is necessary to take into consideration the previous thermomechanical history of the base material. This effect is less likely to be observed in a partial or fully annealed base materials, since the recovery phenomena will not be effective for such short time spans as those observed during fusion welding [48,49].

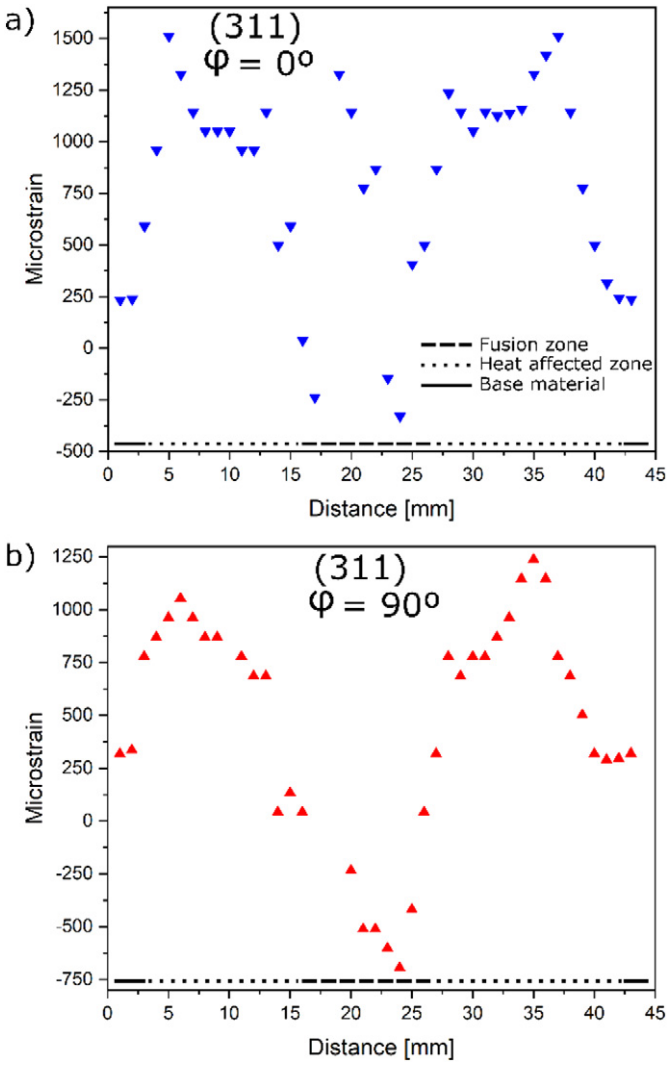

Fig. 11. Evolution of joints microstrain along the longitudinal (a) and transverse (b) directions (refer to Fig. 1) for the (311) diffraction peak.

The microstrain along the welded joints was also determined for the principal directions considering the (311) diffraction peak. These results are depicted in Fig. 11. In the base material, the microstrain is positive along both directions as expected, since rolling imposes a compressive strain through thickness, which is counteracted by tensile strain in the other two normal directions. The peak microstrain occurs in the heat affected zone. In the fusion zone, along the longitudinal direction the microstrain is negative near the fusion boundary, and then sharply increases towards the weld centreline, whereas in the transverse direction the microstrain becomes negative.

The complex microstrain pattern in both directions can be justified based on the imposed thermal cycle, which alter the local mechanical properties during welding. Since no distortion was observed in the as-

Table 1
Summary of the base material and welded joints mechanical properties.

Reference	Yield strength [MPa]	Ultimate tensile strength [MPa]	Fracture strain [%]
Base material	587 ± 7	943 ± 6	9.5 ± 0.2
CrMnFeCoNi welds	248 ± 4	519 ± 3	8.4 ± 0.4

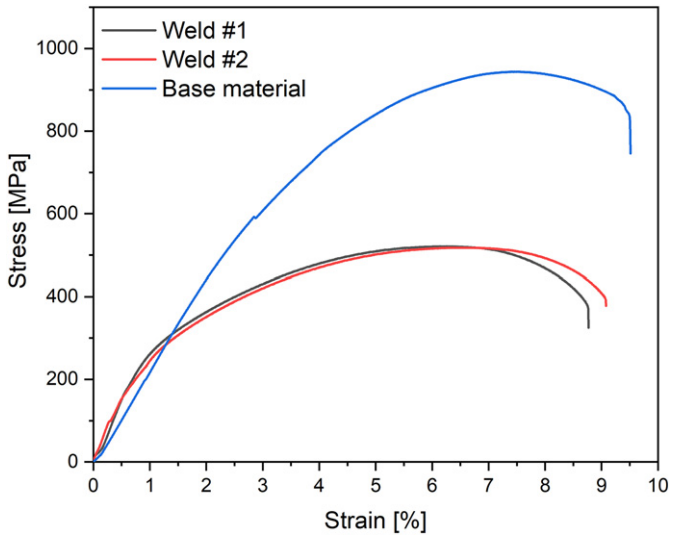

Fig. 12. Representative curves of the mechanical behaviour of the base material and as-welded high entropy alloy joints obtained from tensile testing until failure.

welded plates, this is the most effective way for the material to accommodate the thermal and mechanical strains generated during welding.

3.2. Mechanical properties

In order to assess the mechanical properties of the as-welded CrMnFeCoNi high entropy alloy, mechanical testing until failure was performed. Summary of the mechanical properties of the joints is presented in Table 1. Fig. 12 aims to show the reproductibility in terms of mechanical properties of the welds, while comparing the mechanical behaviour of joints with the base material. A ductile-like behaviour was observed after welding. A decrease in the strenght and ductility of the welded joints compared to the base material is observed and can be justified based on the unfavourable microstructure of the fusion zone, where very large grains and significant material softening were observed. However, the strength of the joints is similar to that reported in [21], where laser welding was used to join a similar alloy composition. Future work will determine the effect of post-weld heat treatments aiming at improving the joints mechanical properties.

Failure of the joints systematically occurred in the fusion zone. Time lapse images taken during mechanical testing clearly show the significant amount of deformation experienced by the fusion zone (refer to Fig. 13). Right before fracture ($t = t_2$ in Fig. 13) it can be perceived that the material will fail in the fusion zone along a line at ≈55° with the tensile direction. This fracture angle is in good agreement with Hill's theory for diffuse and localized necking [54–56].

Failure of the gas tungsten arc welded joints in the fusion zone can be explained based on the previously described microstructural features of this region, namely the large grain size and low hardness. In fact, for most engineering materials, an increase in grain size, as it mainly occurs in the fusion zone, results in a decrease of the material mechanical properties. Additionally, the gradient of microhardness along the joint, with the fusion zone exhibiting a considerably lower hardness (≈150 HV) than in the base material (≈350 HV), will promote a higher strain accumulation in the fusion zone. As such, the fusion zone will deform more extensively than the remaining material until necking, followed by fracture, occurs.

Fracture surface analysis of the welded joints is depicted in Fig. 14. A purely ductile-like fracture, evidenced by the massive presence of dimples, is in good agreement with the significant amount of plastic deformation experienced by the welded joints (refer to Fig. 12).

It has been reported that during deformation of CrMnFeCoNi high entropy alloy nanotwins can be observed at room temperature at engineering strains of ≈28.4% [13]. Because the welded joints fractured ≈8.4% strain, it is expected that the deformation mechanism of the joint is dominated by dislocation plasticity instead of deformation twinning. Future work will envisage the improvement of the mechanical properties of these CrMnFeCoNi welded joints using post-weld heat treatments.

4. Conclusions

Gas tungsten arc welding of a rolled CrMnFeCoNi high entropy alloy was performed. The following conclusions can be drawn:

- overall the CrMnFeCoNi high entropy alloy exhibits good weldability, as no welding defects were observed in the joints;
- recovery, recrystallization and grain growth phenomena were observed to occur in the heat affected zone due to the welding thermal cycle;
- using synchrotron X-ray diffraction experiments it was observed that the effective extension of the heat affected zone is slightly larger than that obtained via conventional electron microscopy or hardness testing;
- mechanical testing of the joints revealed high tensile strength, though a decrease in the joint fracture strain of the joint occurred due to the large grain size and low hardness of the fusion zone, which promote higher strain accumulation in this region.
- The joints have a lower strength and ductility than the base material.

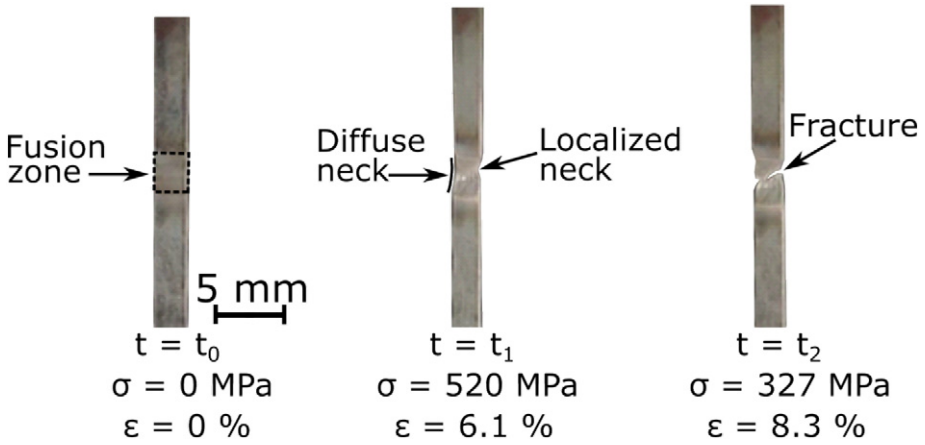

Fig. 13. Evolution of the joint reduced cross section during tensile testing to failure. $t = t_0$ ➔ before any load imposed; $t = t_1$ ➔ onset for necking in the fusion zone; $t = t_2$ ➔ fracture at the weld centreline.

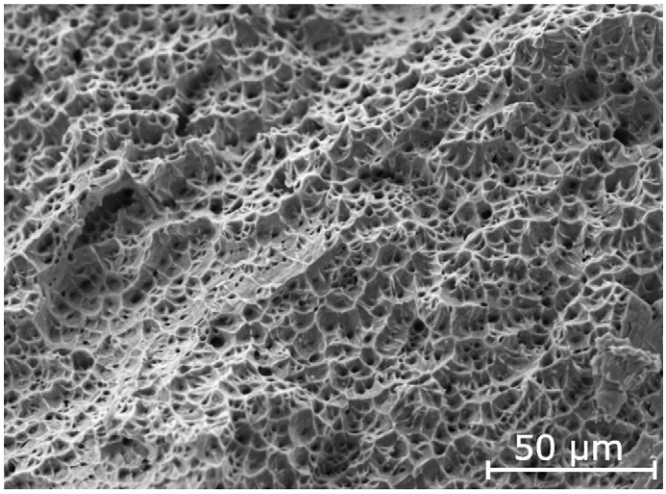

Fig. 14. Fracture surface of the gas tungsten arc welded CrMnFeCoNi high entropy alloy.

Post-weld heat treatment may be the key to improve the joints mechanical performance.

The raw/processed data required to reproduce these findings cannot be shared at this time as the data also forms part of an ongoing study.

CRediT authorship contribution statement

J.P. Oliveira: Conceptualization, Data curation, Formal analysis, Project administration, Supervision, Writing - original draft. **T.M. Curado:** Investigation, Data curation. **Z. Zeng:** Investigation, Data curation, Writing - review & editing. **J.G. Lopes:** Investigation. **Emma Rossinyol:** Investigation, Data curation. **Jeong Min Park:** Investigation, Data curation. **N. Schell:** Investigation, Data curation, Writing - review & editing. **F.M. Braz Fernandes:** Resources, Writing - review & editing. **Hyoung Seop Kim:** Resources, Investigation, Writing - review & editing.

Declaration of competing interest

The authors declare that they have no known competing financial interests or personal relationships that could have appeared to influence the work reported in this paper.

Acknowledgements

JPO, TC and JGL acknowledge Fundação para a Ciência e Tecnologia (FCT) for its financial support through the project UID/EMS/00667/2019 (UNIDEMI). FMBF acknowledges funding of CENIMAT by FEDER through the program COMPETE 2020 and National Funds through FCT-Portuguese Foundation for Science and Technology, under the project UID/CTM/50025/2019 and FCT/MCTES. This work was supported by the Future Material Discovery Project of the National Research Foundation of Korea (NRF) funded by the Ministry of Science and ICT of Korea (NRF-2016M3D1A1023383). Parts of this research were carried out at the High Energy Materials Science (HEMS) P07 beamline at DESY, a member of the Helmholtz Association (HGF). The research leading to this result has been supported by the project CALIPSOplus under the Grant Agreement 730872 from the EU Framework Programme for Research and Innovation HORIZON 2020 (project reference I-20190492 EC). This project has received funding from the EU-H2020 research and innovation programme under grant agreement no. 654360 having benefitted from the access provided by Universitat Autonoma de Barcelona, Consejo Superior de Investigaciones Científicas - Centro Nacional de Microelectrónica in Barcelona (Spain) and DESY at P07 beamline in Hamburg (Germany) within the framework of the NFFA-Europe Transnational Access Activity (project reference Nf-20010136 EC and ID-806).

References

[1] Y. Zhang, T.T. Zuo, Z. Tang, M.C. Gao, K.A. Dahmen, P.K. Liaw, Z.P. Lu, Microstructures and properties of high-entropy alloys, Prog. Mater. Sci. 61 (2014) 1–93, https://doi.org/10.1016/j.pmatsci.2013.10.001.
[2] J. Chen, X. Zhou, W. Wang, B. Liu, Y. Lv, W. Yang, D. Xu, Y. Liu, A review on fundamental of high entropy alloys with promising high–temperature properties, J. Alloys Compd. 760 (2018) 15–30, https://doi.org/10.1016/j.jallcom.2018.05.067.
[3] B. Cantor, I.T.H. Chang, P. Knight, A.J.B. Vincent, Microstructural development in equiatomic multicomponent alloys, Mater. Sci. Eng. A 375–377 (2004) 213–218, https://doi.org/10.1016/j.msea.2003.10.257.
[4] J.W. Yeh, S.K. Chen, S.J. Lin, J.Y. Gan, T.S. Chin, T.T. Shun, C.H. Tsau, S.Y. Chang, Nanostructured high-entropy alloys with multiple principal elements: novel alloy design concepts and outcomes, Adv. Eng. Mater. 6 (2004) 299–303+274, https://doi.org/10.1002/adem.200300567.
[5] Z. Li, S. Zhao, R.O. Ritchie, M.A. Meyers, Mechanical properties of high-entropy alloys with emphasis on face-centered cubic alloys, Prog. Mater. Sci. 102 (2019) 296–345, https://doi.org/10.1016/j.pmatsci.2018.12.003.
[6] L.R. Owen, E.J. Pickering, H.Y. Playford, H.J. Stone, M.G. Tucker, N.G. Jones, An assessment of the lattice strain in the CrMnFeCoNi high-entropy alloy, Acta Mater. 122 (2017) 11–18, https://doi.org/10.1016/j.actamat.2016.09.032.
[7] B. Gludovatz, E.P. George, R.O. Ritchie, Processing, microstructure and mechanical properties of the CrMnFeCoNi high-entropy alloy, Jom 67 (2015) 2262–2270, https://doi.org/10.1007/s11837-015-1589-z.
[8] G. Laplanche, U.F. Volkert, G. Eggeler, E.P. George, Oxidation behavior of the CrMnFeCoNi high-entropy alloy, Oxid. Met. 85 (2016) 629–645, https://doi.org/10.1007/s11085-016-9616-1.
[9] S. Park, H. Nam, Y. Na, H. Kim, Y. Moon, N. Kang, Effect of initial grain size on friction stir weldability for rolled and cast CoCrFeMnNi high - entropy alloys, Met. Mater. Int. (2019) https://doi.org/10.1007/s12540-019-00466-1.
[10] M. Laurent-Brocq, A. Akhatova, L. Perrière, S. Chebini, X. Sauvage, E. Leroy, Y. Champion, Insights into the phase diagram of the CrMnFeCoNi high entropy alloy, Acta Mater. 88 (2015) 355–365, https://doi.org/10.1016/j.actamat.2015.01.068.
[11] J. Gu, M. Song, Annealing-induced abnormal hardening in a cold rolled CrMnFeCoNi high entropy alloy, Scr. Mater. 162 (2019) 345–349, https://doi.org/10.1016/j.scriptamat.2018.11.042.
[12] D. Yim, P. Sathiyamoorthi, S.J. Hong, H.S. Kim, Fabrication and mechanical properties of TiC reinforced CoCrFeMnNi high-entropy alloy composite by water atomization and spark plasma sintering, J. Alloys Compd. 781 (2019) 389–396, https://doi.org/10.1016/j.jallcom.2018.12.119.
[13] G. Laplanche, A. Kostka, O.M. Horst, G. Eggeler, E.P. George, Microstructure evolution and critical stress for twinning in the CrMnFeCoNi high-entropy alloy, Acta Mater. 118 (2016) 152–163, https://doi.org/10.1016/j.actamat.2016.07.038.
[14] P. Penner, L. Liu, a Gerlich, Y. Zhou, Feasibility study of resistance spot welding of dissimilar Al/Mg combinations with Ni based interlayers, Sci. Technol. Weld. Join. 18 (2013) 541–550. doi:https://doi.org/10.1179/1362171813Y.0000000129.
[15] M. Sun, S.T. Niknejad, G. Zhang, M.K. Lee, L. Wu, Y. Zhou, Microstructure and mechanical properties of resistance spot welded AZ31/AA5754 using a nickel interlayer, Mater. Des. 87 (2015) 905–913, https://doi.org/10.1016/j.matdes.2015.08.097.
[16] H. Nam, C. Park, J. Moon, Y. Na, H. Kim, N. Kang, Laser weldability of cast and rolled high-entropy alloys for cryogenic applications, Mater. Sci. Eng. A 742 (2019) 224–230, https://doi.org/10.1016/j.msea.2018.11.009.
[17] N. Kashaev, V. Ventzke, N. Petrov, M. Horstmann, S. Zherebtsov, D. Shaysultanov, V. Sanin, N. Stepanov, Fatigue behaviour of a laser beam welded CoCrFeNiMn-type high entropy alloy, Mater. Sci. Eng. A 766 (2019), 138358. https://doi.org/10.1016/j.msea.2019.138358.
[18] H. Nam, C. Park, C. Kim, H. Kim, N. Kang, Effect of post weld heat treatment on weldability of high entropy alloy welds, Sci. Technol. Weld. Join. 23 (2018) 420–427, https://doi.org/10.1080/13621718.2017.1405564.
[19] H. Nam, S. Park, E. Chun, H. Kim, Laser dissimilar weldability of cast and rolled CoCrFeMnNi high-entropy alloys for cryogenic applications, Sci. Technol. Weld. Join. 0 (2019) 1–8, https://doi.org/10.1080/13621718.2019.1644471.
[20] N. Kashaev, V. Ventzke, N. Stepanov, D. Shaysultanov, V. Sanin, S. Zherebtsov, Laser beam welding of a CoCrFeNiMn-type high entropy alloy produced by self-propagating high-temperature synthesis, Intermetallics 96 (2018) 63–71, https://doi.org/10.1016/j.intermet.2018.02.014.
[21] Z. Wu, S.A.A. David, Z. Feng, H. Bei, Weldability of a high entropy CrMnFeCoNi alloy, Scr. Mater. 124 (2016) 81–85, https://doi.org/10.1016/j.scriptamat.2016.06.046.
[22] J.P. Oliveira, N. Schell, N. Zhou, L. Wood, O. Benafan, Laser welding of precipitation strengthened Ni-rich NiTiHf high temperature shape memory alloys: microstructure and mechanical properties, Mater. Des. 162 (2019) 229–234, https://doi.org/10.1016/j.matdes.2018.11.053.
[23] A. Shamsolhodaei, Y.N. Zhou, A. Michael, Enhancement of mechanical and functional properties of welded NiTi by controlling nickel vapourisation, Sci. Technol. Weld. Join. 0 (2019) 1–7, https://doi.org/10.1080/13621718.2019.1595926.
[24] J.P. Oliveira, B. Crispim, Z. Zeng, T. Omori, F.M. Braz Fernandes, R.M. Miranda, Microstructure and mechanical properties of gas tungsten arc welded Cu-Al-Mn shape

memory alloy rods, J. Mater. Process. Technol. (2019) https://doi.org/10.1016/j.jmatprotec.2019.03.020.
[25] A.M. Torbati, R.M. Miranda, L. Quintino, S. Williams, D. Yapp, Optimization procedures for GMAW of bimetal pipes, J. Mater. Process. Technol. 211 (2011) 1112–1116, https://doi.org/10.1016/j.jmatprotec.2011.01.013.
[26] G.D. Janaki Ram, A. Venugopal Reddy, K. Prasad Rao, G. Madhusudhan Reddy, Control of laves phase in Inconel 718 GTA welds with current pulsing, Sci. Technol. Weld. Join. 9 (2004) 390–398, https://doi.org/10.1179/136217104225021788.
[27] D. Shaysultanov, N. Stepanov, S. Malopheyev, I. Vysotskiy, V. Sanin, S. Mironov, R. Kaibyshev, G. Salishchev, S. Zherebtsov, Friction stir welding of a carbon-doped CoCrFeNiMn high-entropy alloy, Mater. Charact. 145 (2018) 353–361, https://doi.org/10.1016/j.matchar.2018.08.063.
[28] M.G. Jo, H.J. Kim, M. Kang, P.P. Madakashira, E.S. Park, J.Y. Suh, D.I. Kim, S.T. Hong, H.N. Han, Microstructure and mechanical properties of friction stir welded and laser welded high entropy alloy CrMnFeCoNi, Met. Mater. Int. 24 (2018) 73–83, https://doi.org/10.1007/s12540-017-7248-x.
[29] Z.G. Zhu, Y.F. Sun, M.H. Goh, F.L. Ng, Q.B. Nguyen, H. Fujii, S.M.L. Nai, J. Wei, C.H. Shek, Friction stir welding of a CoCrFeNiAl0.3 high entropy alloy, Mater. Lett. 205 (2017) 142–144, https://doi.org/10.1016/j.matlet.2017.06.073.
[30] J. Unfried-Silgado, A.J. Ramirez, Modeling and characterization of as-welded microstructure of solid solution strengthened Ni-Cr-Fe alloys resistant to ductility-dip cracking part II: microstructure characterization, Met. Mater. Int. 20 (2014) 307–315, https://doi.org/10.1007/s12540-014-1022-0.
[31] T. Yuan, Z. Luo, S. Kou, Grain refining of magnesium welds by arc oscillation, Acta Mater. 116 (2016) 166–176, https://doi.org/10.1016/j.actamat.2016.06.036.
[32] A.C. Martin, C. Fink, Initial weldability study on Al 0.5 CrCoCu 0.1 FeNi high-entropy alloy, Weld. World. 63 (2019) 739–750, https://doi.org/10.1007/s40194-019-00702-7.
[33] C.A. Biffi, R. Casati, B. Previtali, A. Tuissi, Microstructure and mechanical properties of laser welded beads realized for joining CuZn open cellular foams, Mater. Lett. 181 (2016) 132–135, https://doi.org/10.1016/j.matlet.2016.05.161.
[34] H. Di, Q. Sun, X. Wang, J. Li, Microstructure and properties in dissimilar/similar weld joints between DP780 and DP980 steels processed by fiber laser welding, J. Mater. Sci. Technol. 33 (2017) 1561–1571, https://doi.org/10.1016/j.jmst.2017.09.001.
[35] P. Staron, T. Fischer, T. Lippmann, A. Stark, S. Daneshpour, D. Schnubel, E. Uhlmann, R. Gerstenberger, B. Camin, W. Reimers, E. Eidenberger, H. Clemens, N. Huber, A. Schreyer, In situ experiments with synchrotron high-energy X-rays and neutrons, Adv. Eng. Mater. 13 (2011) 658–663, https://doi.org/10.1002/adem.201000297.
[36] K.-D. Liss, A. Bartels, A. Schreyer, H. Clemens, High-energy X-rays: a tool for advanced bulk investigations in materials science and physics, Textures Microstruct 35 (2003) 219–252, https://doi.org/10.1080/07303300310001634952.
[37] J.P. Oliveira, F.M. Braz Fernandes, R.M. Miranda, N. Schell, J.L. Ocaña, Effect of laser welding parameters on the austenite and martensite phase fractions of NiTi, Mater. Charact. 119 (2016) 148–151, https://doi.org/10.1016/j.matchar.2016.08.001.
[38] S.A.A.A. Mousavi, S.T. Niknejad, Study on the microstructure and mechanical properties of Nd:YAG pulsed laser beam weld of UNS-C17200 copper beryllium alloy, J. Mater. Process. Technol. 210 (2010) 1472–1481, https://doi.org/10.1016/j.jmatprotec.2010.04.005.
[39] J.D. Escobar, G.A. Faria, L. Wu, J.P. Oliveira, P.R. Mei, A.J. Ramirez, Austenite reversion kinetics and stability during tempering of a Ti-stabilized supermartensitic stainless steel: correlative in situ synchrotron X-ray diffraction and dilatometry, Acta Mater. 138 (2017) 92–99, https://doi.org/10.1016/j.actamat.2017.07.036.
[40] A.P. Hammersley, S.O. Svensson, M. Hanfland, A.N. Fitch, D. Hausermann, Two-dimensional detector software: from real detector to idealised image or two-theta scan, High Pressure Res. 14 (1996) 235–248, https://doi.org/10.1080/08957959608201408.
[41] A.P. Hammersley, S.O. Svensson, A. Thompson, Calibration and correction of spatial distortions in 2D detector systems, Nucl. Instruments Methods Phys. Res. Sect. A Accel. Spectrometers, Detect. Assoc. Equip, 346, 1994, pp. 312–321, https://doi.org/10.1016/0168-9002(94)90720-X.
[42] J.P. Oliveira, J.F. Duarte, P. Inácio, N. Schell, R.M. Miranda, T.G. Santos, Production of Al/NiTi composites by friction stir welding assisted by electrical current, Mater. Des. 113 (2017) 311–318, https://doi.org/10.1016/j.matdes.2016.10.038.
[43] A.M. Korsunsky, S.P. Collins, R. Alexander Owen, M.R. Daymond, S. Achtioui, K.E. James, Fast residual stress mapping using energy-dispersive synchrotron X-ray diffraction on station 16.3 at the SRS, J. Synchrotron Radiat. 9 (2002) 77–81, https://doi.org/10.1107/S0909049502001905.
[44] L. Ma, L. Wang, Z. Nie, F. Wang, Y. Xue, J. Zhou, T. Cao, Y. Wang, Y. Ren, Reversible deformation-induced martensitic transformation in Al0.6CoCrFeNi high-entropy alloy investigated by in situ synchrotron-based high-energy X-ray diffraction, Acta Mater. 128 (2017) 12–21, https://doi.org/10.1016/j.actamat.2017.02.014.
[45] M. Zhang, L. Li, J. Ding, Q. Wu, Y.D. Wang, J. Almer, F. Guo, Y. Ren, Temperature-dependent micromechanical behavior of medium-Mn transformation-induced-plasticity steel studied by in situ synchrotron X-ray diffraction, Acta Mater. 141 (2017) 294–303, https://doi.org/10.1016/j.actamat.2017.09.030.
[46] P. Thompson, D.E. Cox, J.B. Hastings, Rietveld refinement of Debye–Scherrer synchrotron X-ray data from Al2O3, J. Appl. Crystallogr. 20 (1987) 79–83, https://doi.org/10.1107/S0021889887087090.
[47] S. Kou, Welding Metallurgy, 2nd ed John Wiley & Sons, Inc., Hoboken, 2002https://doi.org/10.1002/0471434027.
[48] S.A. David, S.S. Babu, J.M. Vitek, Welding: solidification and microstructure, JOM 55 (2003) 14–20, https://doi.org/10.1007/s11837-003-0134-7.
[49] T. DebRoy, S.A. David, Physical processes in fusion welding, Rev. Mod. Phys. 67 (1995) 85–112, https://doi.org/10.1103/RevModPhys.67.85.
[50] E.J. Pickering, R. Muñoz-Moreno, H.J. Stone, N.G. Jones, Precipitation in the equiatomic high-entropy alloy CrMnFeCoNi, Scr. Mater. 113 (2016) 106–109, https://doi.org/10.1016/j.scriptamat.2015.10.025.
[51] J.P. Oliveira, D. Barbosa, F.M.B. Fernandes, R.M. Miranda, Tungsten inert gas (TIG) welding of Ni-rich NiTi plates: functional behavior, Smart Mater. Struct. 25 (2016) 03LT01, https://doi.org/10.1088/0964-1726/25/3/03LT01.
[52] G. Laplanche, O. Horst, F. Otto, G. Eggeler, E.P. George, Microstructural evolution of a CoCrFeMnNi high-entropy alloy after swaging and annealing, J. Alloys Compd. 647 (2015) 548–557. https://doi.org/10.1016/j.jallcom.2015.05.129.
[53] M.V. Klimova, D.G. Shaysultanov, S.V. Zherebtsov, N.D. Stepanov, Effect of second phase particles on mechanical properties and grain growth in a CoCrFeMnNi high entropy alloy, Mater. Sci. Eng. A 748 (2019) 228–235, https://doi.org/10.1016/j.msea.2019.01.112.
[54] R. Hill, The Mathematical Theory of Plasticity, Clarendon Press, 1998.
[55] F.A. McClintock, Z.M. Zheng, Ductile fracture in sheets under transverse strain gradients, Int. J. Fract. 64 (1993) 321–337, https://doi.org/10.1007/BF00017848.
[56] C. Li, E. Daxin, N. Yi, Analysis on fracture initiation and fracture angle in ductile sheet metal under uniaxial tension by experiments and finite element simulations, J. Mater. Res. 31 (2016) 3991–3999, https://doi.org/10.1557/jmr.2016.412.